Journal of Constructional Steel Research 159 (2019) 147–160

Contents lists available at ScienceDirect

Journal of Constructional Steel Research

# Beam-tendon finite elements for post-tensioned steel-concrete composite beams with partial interaction

João Batista M. Sousa Jr. *, Evandro Parente Jr., Ésio M.F. Lima, Michelle V.X. Oliveira

*Computational Mechanics Lab, Dept. Structural Engineering, Universidade Federal do Ceará, Campus do Pici - Bloco 728, Fortaleza, CE 60440-900, Brazil*

ARTICLE INFO

*Article history:*
Received 10 January 2019
Received in revised form 5 April 2019
Accepted 5 April 2019
Available online 29 April 2019

*Keywords:*
Prestressed composite beam
Partial interaction
Post-tensioned composite beam

ABSTRACT

Although prestressing is a technique usually linked to reinforced concrete structures, composite steel-concrete beams may improve their mechanical behaviour through post-tensioning tendons. A particular feature of composite beams is the possibility of slip or partial interaction between the components as a result of the shear connection flexibility. This paper describes the development, implementation and test of a one-dimensional finite element formulation for the nonlinear analysis of steel-concrete composite beams prestressed by external tendons, fixed at discrete points along the steel component, taking into account the partial interaction between steel and concrete. Physical and geometrical nonlinearities are considered and a consistent derivation of the tangent stiffness matrix for the tendon is introduced. A recently developed procedure for state determination after prestressing operation is adapted for partially connected composite beams prestressed by external tendons. The accuracy and robustness of the finite element formulation is assessed by means of the comparison with a comprehensive series of experimental results.



## 1. Introduction

Prestressing techniques have been traditionally associated with concrete structures. However, steel and composite steel-concrete structures may benefit strongly from the application of stress states induced by prestressing prior to working loads.

Post-tensioned composite steel-concrete beams present advantages over their non-prestressed counterparts. They display an increase in the range of elastic behavior, as well in yield and ultimate load values [1–3]. In continuous beams, there is reduction of concrete cracking in hogging moment regions. They may also have better fatigue performance [4] if cracking of top slab is prevented. Lighter steel sections may be employed providing economic design [5].

Although post-tensioning on composite beams is mostly present in rehabilitation and repair, its application on a steel-concrete beam before service load results in a very efficient load-carrying system, able to withstand higher loads with reduced deformations and longer spans.

In the steel-concrete composite beam literature, slip (also called interlayer slip) has been employed as a measure to characterize the different displacements between steel and concrete at the level of the connection, due to deformability of the connector device (e.g. shear studs). The terms flexible shear connection and partial interaction, among others, are commonly employed to describe this phenomenon.

A prestressed steel concrete composite beam (PSCCB) may be designed in different ways depending on the section geometry, the position and layout of the tendon and the type of prestressing, as well as construction sequence and propping scheme. The usual scheme of a PSCCB consists of a concrete slab, linked to the steel beam by mechanical shear connectors, and high strength steel cables for the application of prestressing on the steel beam. If post-tensioning is applied after concrete curing, post-tension and load application already takes advantage of the composite cross section.

Research on PSCCBs focused on experimental tests, as well as analytical and numerical approaches, and some of these works are listed below. Saadatmanesh et al. [1] tested PSCCBs where steel beams were prestressed before slab casting under positive and negative bending. Their main conclusions are that the addition of tendons increases the yield and ultimate loads, and that saddle points should be included in order to keep tendon eccentricity to reach the beam ultimate moment. Their results were assessed by a scheme based on full interaction. Ayyub et al. [2] tested three models of PSCCBs with steel beams prestressed before slab casting. The authors concluded that the assumption of zero slip may not be appropriate and inferred that the slip resulted in larger deflections than predicted by their analytical model. Moreover, they found that draped tendons increase ductility. The ultimate resistance of draped and straight tendon beams was similar. Chen and Gu [3] carried out tests of two PSCCBs, and measured deflections, tendon strains, midspan strains and slips at the beam ends. Lorenc and Kubica [6] carried out experimental tests on six composite beams, five of them prestressed, with draped and straight tendons, and

* Corresponding author.
*E-mail address:* joaobatistasousajr@ufc.br (J.B.M. Sousa).

https://doi.org/10.1016/j.jcsr.2019.04.009
0143-974X/

produced a comprehensive collection of test results, such as displacements, slips, strains on concrete and steel, drawing several conclusions on PSCCBs behaviour under static loads. Furthermore, they carried out push-out tests to characterize the connection load-slip relationship. Among other conclusions from the tests, they found that the tendon layout did not influence the ultimate capacity and the steel-concrete adherence at the contact surface furnished a considerable part of the connection strength before ultimate loads, leading to difficulties of slip prediction.

Analytical formulations were developed to find closed-form expressions to capture the behaviour of PSCCB's. Based on equilibrium, compatibility, and assuming plastic distribution of stress, Chen and Gu [3] obtained simplified expressions for the ultimate incremental tendon stress and ultimate beam moment for four tendon layout cases were derived. Saadatmanesh and coworkers [7] developed expressions for the behaviour of PSCCB's which agreed well with their test data. Formulas for calculating the three characteristic loads (crack, yield, and ultimate loads) of two-span prestressed continuous composite beams under symmetric concentrated loads were proposed and extended to general cases by Nie et al. [8].

In order to develop a reliable numerical analysis of such structures, one should consider the material and geometrical nonlinearities, the interaction between beam and tendon, the slip beteween steel beam and concrete slab and possibly the long-term effects. Moreover, the multistep nature of the system, involving a sequence of post-tensioning operations and load application [9], poses additional requirements. In particular, the increase in tendon strain is dependent on the deformation of the whole member and the tendon stress cannot be determined by a single section analysis. Moreover, the effective tendon lever arms would change with member deflections, mainly in the absence of deviator points, which must be taken into account as part of the geometric nonlinearity [10].

The numerical simulation of postensioned beams has been investigated by several authors. The post-tensioning step is a matter of interest in itself, either applied to RC or composite beams. Two main approaches may be identified: The equivalent load scheme, where the tendon is treated as an external member and introduced as an applied force, and the load-resisting approach, where the tendon is part of the structure and its forces are dealt with the discretization of the tendon along with the beam. In any case, nonlinear geometric and material effects play a significant role and should be taken into account.

Chen and Gu [3] presented FE analyses of their experiment (beam B2). The concrete slab, steel flanges and web was modeled using large deformation shell elements, shear connectors by spring-link elements and the tendons by beam elements. Dall'Asta, Zona and coworkers [10,11] developed a one-dimensional FE model for externally prestressed composite beams with deformable connection and linear geometric assumptions. Later the same group [12,13] extended the analytical and numerical formulations for large displacement problems tackling the nonlinear effects that the displacements of the tendon produce on the equilibrium of the beam, for concrete and composite beams. They also presented a rigorous discussion on the possibilities of simplifications, under the small strain and moderate rotation theory, which is adopted in the present work. Lou, Lopes and Lopes [14] presented a FE beam model for PSCCB's subjected to long-term loads, enabling the consideration of creep and shrinkage, for full interaction assumptions. Nie et al. [8] employed a robust commercial finite element scheme to assess their analytical formulaes. Mohamed and coworkers [15] developed a 3D model using ANSYS and investigated the effect of variations of geometrical properties on the strength of PSCCB's. The studied parameters include different cases of loading, tendon profiles, beam spans, initial prestressing levels and different dimensions of steel sections and concrete deck, for different tendon layouts. Other works on PSCCB's based on nonlinear static 3D analysis were recently published [16,17].

The purpose of the present paper is to present the development, implementation and test of a specialized 1D finite elements for the nonlinear analysis of PSCCBs under static short-term loading. The analysis takes into account the relative displacements between steel and concrete, named as partial interaction, partial shear connection or interlayer slip. The treatment of the prestressing step is discussed in detail and is carried out by the algorithm recently developed by Moreira et al. [18] adapted for external prestressing of tendons with or without deviators, and partially connected composite beams. The tendon is considered as a load-resisting element which contributes to the overall internal force and stiffness matrix, and assumed to slide without friction along deviators. Nonlinear material and geometric effects are dealt with providing a consistent tangent stiffness with excellent convergence properties. The assessment of the numerical scheme is carried out by comparison of results of experimental tests on composite steel-concrete beams.

## 2. Beam FE formulation

Despite improvements on computational resources, one-dimensional finite elements still play an important role among other possibilities of numerical modeling, due to their simplicity of formulation and implementation, as well as their fair compromise between computing costs and precision of results.

Composite beams under partial interaction have been the focus of intense research in the last decades and their numerical analysis by the FE method is the subject of a great amount of published work. Many different formulations for beam elements have already been implemented and tested, and some of the related works are presented in the following.

The requirement for the analysis of PSCCB is a robust beam-column FE for nonlinear analysis which takes into account partial interaction. A very common framework is the Euler-Bernoulli (EB) beam model combined with Newmark composite beam theory, which usually provides good results for slender beams. One of the first elements of such type for nonlinear analysis was developed by Dall'Asta and Zona [19]. Several other formulations have been proposed since, with improvements on topics such as physical and geometric nonlinearity, employment of alternative force-based formulations, elements based on the analytical solutions and many more [9,20–26]. This is still an active area of research.

The chosen model in this work is based on a nonlinear EB model, described by Sousa Jr. et al. [27]. This is a displacement-based element with cubic (hermitian) interpolation of transverse displacements and quadratic interpolation of axial displacements. The steel and concrete beams may have any symmetric cross section, and the transverse displacement and rotation are shared between the upper and lower components. It has been shown that this choice of interpolants avoids the slip locking which appears in some FE for beams with interlayer slip and provides excellent results in linear as well as nonlinear analyses.

A brief description of the FE formulation follows. The in-plane beam displacements $U_\alpha(x,y)$ and $V_\alpha(x,y)$, where $\alpha$ is either $c$ or $s$ for the upper (concrete) or lower (steel) sections respectively, are expressed as

$$U_\alpha(x,y) = u_\alpha(x) - y_\alpha\ \theta(x) = u_\alpha(x) - y_\alpha\ v_{,x} \tag{1}$$

where $y_\alpha$ is a section local axis, not necessarily centroidal, and

$$V_\alpha(x,y) = v(x) \tag{2}$$

For the slip at the connection, one gets

$$s(x) = u_c(x) - u_s(x) - h\ v_{,x} \tag{3}$$

Under EB assumptions, only the axial strain $\varepsilon_x$ and corrresponding stress $\sigma_x$ are considered for each component, and for small strain-

moderate rotation theory [12], the strains are given by

$$\varepsilon_{x\alpha} = u_{\alpha,x} - y_\alpha \; v_{,xx} + \frac{1}{2}(v_{,x})^2 \tag{4}$$

The last term is responsible for the nonlinear geometric effects. With the membrane and bending terms the strain may also be expressed as

$$\varepsilon_{x\alpha} = \varepsilon_{0\alpha} - y_\alpha \; \kappa \tag{5}$$

with $\kappa = v_{,xx}$ defined as the curvature. The shear connection is assumed to have a nonlinear force-slip relationship of the type $S = S(s)$, where $S$ means the connection force per unit length. Proper expressions for the connection behaviour are discussed later.

The internal virtual work is given by the sum of the contributions of the steel and concrete components plus the shear connection

$$\delta W_{int} = \int_0^{\ell} \left( \sum_{\alpha=1,2} \int_{A_\alpha} \delta\varepsilon_{x\alpha}\sigma_{x\alpha} \mathrm{d}A_\alpha + \delta s S \right) \mathrm{d}x \tag{6}$$

and leads to the internal force vector in the FE context.

From the definition of the axial strain (4), the incremental strain is given by

$$\delta\varepsilon_{x\alpha} = \delta u_{\alpha,x} - y_\alpha \; \delta v_{,xx} + v_{,x} \; \delta v_{,x} \tag{7}$$

Introducing (7) in the internal virtual work expression, and defining the normal force and bending moment on each component as

$$N_\alpha = \int_{A_\alpha} \sigma_{x\alpha} \mathrm{d}A_\alpha \tag{8}$$

$$M_\alpha = -\int_{A_\alpha} \sigma_{x\alpha} y_\alpha \mathrm{d}A_\alpha \tag{9}$$

the internal virtual work may be rewritten in matrix form as

$$\delta W_{int} = \int_0^{\ell} \delta\boldsymbol{\varepsilon}^t \boldsymbol{\sigma} \mathrm{d}x \tag{10}$$

with the generalized stresses and strains given by

$$\boldsymbol{\varepsilon}^T = [\varepsilon_{0c} \;\; \varepsilon_{0s} \;\; \kappa \;\; s] \qquad \text{and} \qquad \boldsymbol{\sigma}^T = [N_c \;\; N_s \;\; M \;\; S] \tag{11}$$

with $M = M_c + M_s$. Collecting the displacements in vector $\mathbf{u}$

$$\mathbf{u}^T = [u_c \;\; u_s \;\; v] \tag{12}$$

the generalized strains are given by

$$\boldsymbol{\varepsilon} = \partial\mathbf{u} \tag{13}$$

with matrix $\boldsymbol{\partial}$ given by

$$\partial = \begin{bmatrix} \partial_x & 0 & \frac{1}{2}v_{,x} \; \partial_x \\ 0 & \partial_x & \frac{1}{2}v_{,x} \; \partial_x \\ 0 & 0 & -\partial_{xx} \\ -1 & 1 & -h \; \partial_x \end{bmatrix} \tag{14}$$

The generalized strain variations are given in a similar fashion by

$$\delta\boldsymbol{\varepsilon} = \overline{\partial}\delta\mathbf{u} \tag{15}$$

with matrix $\overline{\partial}$ identical to $\boldsymbol{\partial}$ except from the terms $\frac{1}{2}$ which are not present in $\overline{\partial}_{13}$ and $\overline{\partial}_{23}$.

To carry out the development of the FE formulation the displacement interpolation must be defined. For the axial $u_c$, $u_s$ and transverse $v$ displacements the interpolation functions $\boldsymbol{\Phi}_u$ and $\boldsymbol{\Phi}_v$ are introduced with identical interpolations for virtual quantities $\delta u_\alpha$ and $\delta v$. Functions $\boldsymbol{\Phi}_u$ are quadratic to circumvent the slip locking problem. Functions $\boldsymbol{\Phi}_v$ must reflect continuity of $v$ and its first derivative, therefore hermite polynomials are used. Fig. 1 shows the element degrees of freedom. The matrix expression for the displacement interpolation is

$$\boldsymbol{u}(x) = \boldsymbol{\Phi}(x)\boldsymbol{d} \tag{16}$$

where

$$\boldsymbol{u}^T = \{ u_c \quad u_s \quad v \} \tag{17}$$

$$\Phi = \begin{bmatrix} \Phi_{u\mathbf{1}} & \mathbf{0} & \mathbf{0} & \mathbf{0} & \Phi_{u\mathbf{2}} & \mathbf{0} & \Phi_{u\mathbf{3}} & \mathbf{0} & \mathbf{0} & \mathbf{0} \\ \mathbf{0} & \Phi_{u\mathbf{1}} & \mathbf{0} & \mathbf{0} & \mathbf{0} & \Phi_{u\mathbf{2}} & \mathbf{0} & \Phi_{u\mathbf{3}} & \mathbf{0} & \mathbf{0} \\ \mathbf{0} & \mathbf{0} & \Phi_{v\mathbf{1}} & \Phi_{v\mathbf{2}} & \mathbf{0} & \mathbf{0} & \mathbf{0} & \mathbf{0} & \Phi_{v\mathbf{3}} & \Phi_{v\mathbf{4}} \end{bmatrix} \tag{18}$$

$$\boldsymbol{d}^T = \{ u_{c1} \quad u_{s1} \quad v_1 \quad \theta_1 \quad u_{c2} \quad u_{s2} \quad u_{c3} \quad u_{s3} \quad v_2 \quad \theta_2 \} \tag{19}$$

Employing the displacement interpolation one gets for the total strains

$$\boldsymbol{\varepsilon} = (\boldsymbol{\partial}\Phi)\mathbf{d} = \mathbf{B}\mathbf{d} \tag{20}$$

and for the incremental strains

$$\delta\boldsymbol{\varepsilon} = \left(\overline{\boldsymbol{\partial}}\Phi\right)\delta\mathbf{d} = \overline{\mathbf{B}}\delta\mathbf{d} \tag{21}$$

where the strain-displacement matrices $\mathbf{B}$, $\overline{\mathbf{B}}$ may be written as

$$\boldsymbol{B} = \boldsymbol{B}_0 + \frac{1}{2}\boldsymbol{B}_L \qquad\qquad \overline{\boldsymbol{B}} = \boldsymbol{B}_0 + \boldsymbol{B}_L \tag{22}$$

Matrices $\mathbf{B}_0$ and $\mathbf{B}_L$, respectively, are independent of and linear on the nodal displacement vector. It may be easily verified that $\mathbf{B}_0$ is written as

$$\begin{bmatrix} \Phi_{u1,x} & 0 & 0 & 0 & \Phi_{u2,x} & 0 & \Phi_{u3,x} & 0 & 0 & 0 \\ 0 & \Phi_{u1,x} & 0 & 0 & 0 & \Phi_{u2,x} & 0 & \Phi_{u3,x} & 0 & 0 \\ 0 & 0 & \Phi_{v1,xx} & \Phi_{v2,xx} & 0 & 0 & 0 & 0 & \Phi_{v3,xx} & \Phi_{v4,xx} \\ -\Phi_{u1} & \Phi_{u1} & -h\Phi_{v1,x} & -h\Phi_{v2,x} & -\Phi_{u2} & \Phi_{u2} & -\Phi_{u3} & \Phi_{u3} & -h\Phi_{v3,x} & -h\Phi_{v2,x} \end{bmatrix} \tag{23}$$

If the following vector is defined

$$\mathbf{m} = [0 \quad 0 \quad \Phi_{v1,x} \quad \Phi_{v2,x} \quad 0 \quad 0 \quad 0 \quad 0 \quad \Phi_{v3,x} \quad \Phi_{v4,x}] \tag{24}$$

the displacement-dependent matrix $\mathbf{B}_L$ may be written as

$$\begin{bmatrix} \mathbf{d}^T \; \mathbf{m}^T\mathbf{m} \\ \mathbf{d}^T \; \mathbf{m}^T\mathbf{m} \\ \mathbf{0}_{2\times 10} \end{bmatrix} \tag{25}$$

Introduction of the previous terms into the virtual work expression allows the identification of the internal force vector $\mathbf{g}_B$ (subscript $B$ refers to beam)

$$\mathbf{g}_B = \int_0^{\ell} \overline{\mathbf{B}}^T \; \sigma \; \mathrm{d}x = \int_0^{\ell} \left(\overline{\mathbf{B}}_0^T + \overline{\mathbf{B}}_L^T\right) \; \sigma \; \mathrm{d}x \tag{26}$$

The external virtual work is a function of the applied loads (body forces, surface and member end loads). These terms will give rise to

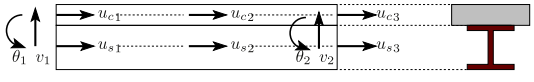


**Fig. 1.** Degrees of freedom for composite beam element.

equivalent loads **r** to be applied to the discrete finite element model and their evaluation follows standard procedures.

The tangent stiffness matrix is obtained from the derivative of the internal force with respect to the displacement vector

$$\mathbf{k}_B = \frac{\partial \mathbf{g}_B}{\partial \mathbf{d}} = \int_0^{\ell} \frac{\partial \overline{\mathbf{B}}^T}{\partial \mathbf{d}} \ \boldsymbol{\sigma} \ \mathrm{d}x + \int_0^{\ell} \overline{\mathbf{B}}^T \ \frac{\partial \boldsymbol{\sigma}}{\partial \mathbf{d}} \ \mathrm{d}x \tag{27}$$

The second integral on the r.h.s. of Eq.(27) is obtained using

$$\frac{\partial \boldsymbol{\sigma}}{\partial \mathbf{d}} = \frac{\partial \boldsymbol{\sigma}}{\partial \boldsymbol{\varepsilon}} \frac{\partial \boldsymbol{\varepsilon}}{\partial \mathbf{d}} = \mathbf{C}\overline{\mathbf{B}} \tag{28}$$

where matrix **C** collects the cross section stiffness coefficients

$$\mathbf{C} = \begin{bmatrix} EA_c & 0 & ES_c & 0 \\ 0 & EA_s & ES_s & 0 \\ ES_c & ES_s & EI_c + EI_s & 0 \\ 0 & 0 & 0 & K \end{bmatrix} \tag{29}$$

which, if $E_t = \frac{\mathrm{d}\sigma}{\mathrm{d}\varepsilon}$ is defined as the material tangent modulus, are defined as

$$EA_\alpha = \frac{\mathrm{d}N_\alpha}{\mathrm{d}\varepsilon_{0\alpha}} = \int_{A_\alpha} E_T \mathrm{d}A_\alpha \tag{30}$$

$$ES_\alpha = \frac{\mathrm{d}N_\alpha}{\mathrm{d}\kappa} = \frac{\mathrm{d}M_\alpha}{\mathrm{d}\varepsilon_{0\alpha}} = -\int_{A_\alpha} E_T y_\alpha \mathrm{d}A_\alpha \tag{31}$$

$$EI_\alpha = \frac{\mathrm{d}M_\alpha}{\mathrm{d}\kappa} = \int_{A_\alpha} E_T y_\alpha^2 \mathrm{d}A_\alpha \tag{32}$$

along with the connection tangent stiffness

$$K = \frac{\mathrm{d}S}{\mathrm{d}s} \tag{33}$$

The integrations in Eqs.(8), (9) and (30)−(32) are influenced by material nonlinearity and may be performed in a number of ways [28]. Numerical integration is usually employed either with Gauss, Gauss-Lobatto or midpoint rules in the so-called fiber method, which in the plane case becomes a layer method, which is employed here.

The first term in the integral on the r.h.s. of Eq.(27) may be written as

$$\left.\frac{\partial\left(\overline{\mathbf{B}}^T\boldsymbol{\sigma}\right)}{\partial \mathbf{d}}\right|_{\boldsymbol{\sigma}=\text{const}} = \frac{\partial}{\partial \mathbf{d}}\left(\overline{\mathbf{B}}_1 N_c + \overline{\mathbf{B}}_2 N_s\right) \tag{34}$$

where $\overline{\mathbf{B}}_i$ is the transpose of the i$^{th}$ line of $\overline{\mathbf{B}}$. Performing the derivatives in Eq.(34) one gets

$$\int_0^{\ell} \frac{\partial \overline{\mathbf{B}}^T}{\partial \mathbf{d}} \ \boldsymbol{\sigma} \ \mathrm{d}x = \int_0^{\ell} (N_c + N_s) \ \mathbf{m}^T\mathbf{m} \ \mathrm{d}x \tag{35}$$

Combining the previous equations the final form of the tangent stiffness matrix for the beam is

$$\mathbf{k}_B = \int_0^{\ell} \overline{\mathbf{B}}^T\mathbf{C}\overline{\mathbf{B}} \ \mathrm{d}x + \int_0^{\ell} (N_c + N_s) \ \mathbf{m}^T\mathbf{m} \ \mathrm{d}x \tag{36}$$

## 3. Material and connection properties

The uniaxial monotonic stress-strain relations for the concrete, the reinforcement and the prestressing tendon are essential for the numerical procedure.

For the concrete component, several stress-strain relations have been proposed, and there is no agreement in the literature as to which one leads to the best numerical behaviour, or even to the best fit of experimental data. Softening, confinement and tension stiffening play important roles on the definition of the relations to be used.

In this work the model from Zupan and Saje [29] is employed. It is composed of a single expression ranging from the ultimate compressive strain in the concrete $\varepsilon_{cu}$ to $\varepsilon_{ctr}$, the value of strain corresponding to the resistance of the concrete in tension, and a straight line from this peak tensile stress to zero, attained at the maximum tensile strain $\varepsilon_{ctu}$:

$$\sigma_c = \begin{cases} f_c \dfrac{2 \mid \varepsilon_{c0} \mid \varepsilon_c}{\varepsilon_{c0}^2 + \varepsilon_c^2} & \varepsilon_{cu} \le \varepsilon_c \le \varepsilon_{ctr} \\ f_{cr} \dfrac{\varepsilon_c - \varepsilon_{ctu}}{\varepsilon_{ctr} - \varepsilon_{ctu}} & \varepsilon_{ctr} \le \varepsilon_c \le \varepsilon_{ctu} \end{cases} \tag{37}$$

This model is numerically convenient as a single smooth expression is used from the tension to the compression ranges, with a straight segment after peak tension stress. The four model input parameters are $\varepsilon_{cu}$, $\varepsilon_{c0}$, $\varepsilon_{ctr}$, $\varepsilon_{ctu}$ and $f_c$, which is concrete compressive resistance.

The constitutive relation adopted for the prestressing steel is that from Menegotto and Pinto [30], given by the single expression valid only in tension

$$\sigma_p = \varepsilon_p E \left[ Q + (1-Q)\left(1 + \left(\frac{E\varepsilon_p}{K\sigma_{py}}\right)^R\right)^{1/R} \right] \le \sigma_{pu} \tag{38}$$

where $E_p$ is the initial elastic modulus, $\sigma_{py}$ is the conventional yield stress (corresponds to a yield strain equal 0.01), and $K$, $Q$ and $R$ are non-dimensional coefficients which may be adjusted to improve fit to experimental data.

A bilinear model is adopted for the reinforcing steel, under either tension or compression:

$$\sigma_s = \begin{cases} -f_y - E_{sh}\left(\varepsilon_s + \varepsilon_{sy}\right) & -\varepsilon_{su} \le \varepsilon_s \le -\varepsilon_{sy} \\ E_s\varepsilon_s & -\varepsilon_{sy} \le \varepsilon_s \le \varepsilon_{sy} \\ f_y + E_{sh}\left(\varepsilon_s - \varepsilon_{sy}\right) & \varepsilon_{sy} \le \varepsilon_s \le \varepsilon_{su} \end{cases} \tag{39}$$

where $E_s$ and $E_{sh}$ are the moduli before and after yielding, $\varepsilon_{sy}$ the yielding strain and $\varepsilon_{su}$ the ultimate strain.

In the described FE model the shear connection, which is essentially a discrete set of mechanical devices, needs to be represented as a continuous nonlinear resisting element. A very well-known expression for the connection behaviour is the Ollgaard relation [31]:

$$F(s) = F_{max} \ \left(1 - e^{-\beta s}\right)^{\alpha} \tag{40}$$

where $F_{max}$ is the connector ultimate resistance, $s$ is the slip and $\beta$, $\alpha$ are parameters to be adjusted. Eq.(40) is numerically unstable as its employment results in infinite connection stiffness for a zero value of slip. To circumvent this issue, in this work a secant linear relation is employed at the vicinity of the origin.

## 4. Tendon FE formulation

Similar to [14,18], the proposed model considers the prestressing tendon as an assemblage of straight segments, but in the present work the tendon is considered as a resisting element, contributing not only to the internal force but also to the tangent stiffness matrix.

The present formulation neglects the friction between tendon and deviators. Therefore, tendon strain $\varepsilon_p$ and stress $\sigma_p$ are considered constant along the tendon length. The endpoints of each straight segment are linked to the steel element degrees of freedom, see Fig. 2. The terms $e_i$, $e_j$ are the vertical distances (eccentricities) between the axis of the steel component and the corresponding tendon point position,

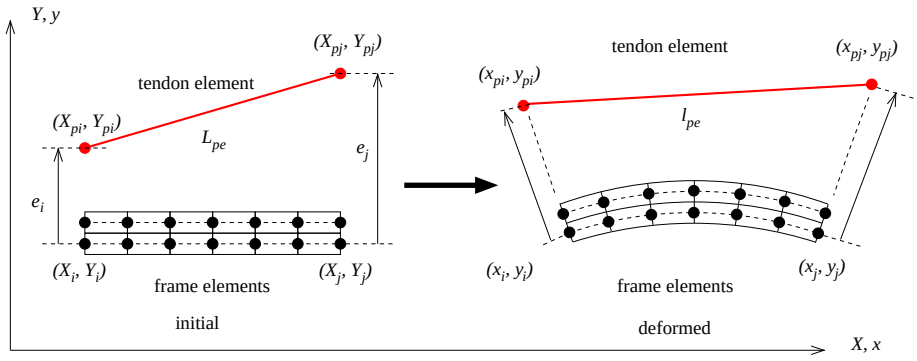


**Fig. 2.** Deformation of tendon and beam elements.

at nodes $i$ and $j$ respectively. It is mandatory that the global mesh has a node at every anchorage or deviator point.

The displacements of the straight tendon segment connecting anchorage or deviation points located at horizontal positions corresponding to nodes $i$ and $j$ are obtained from the displacements of the respective nodes:

$$\begin{aligned} u_{pi} &= x_{pi} - X_{pi} = u_{si} - e_i\,\theta_i \\ v_{pi} &= y_{pi} - Y_{pi} = v_i \\ u_{pj} &= x_{pj} - X_{pj} = u_{sj} - e_j\,\theta_j \\ v_{pj} &= y_{pj} - Y_{pj} = v_j \end{aligned} \tag{41}$$

where $u_{pi}$, $u_{pj}$ are the horizontal and $v_{pi}$, $v_{pj}$ the vertical displacements of the straight segment end points. This is an expression related to the small strain, moderate rotation kinematical assumption which is valid provided that the layout of the cable remains close to the beam, see [13] for a rigorous mathematical analysis.

The previous expression can be written in matrix form as

$$\begin{Bmatrix} u_{pi} \\ v_{pi} \\ u_{pj} \\ v_{pj} \end{Bmatrix} = \begin{bmatrix} 0 & 1 & 0 & -e_i & & & & \\ 0 & 0 & 1 & 0 & & & & \\ & & & & 0 & 1 & 0 & -e_j \\ & & & & 0 & 0 & 1 & 0 \end{bmatrix} \begin{Bmatrix} u_{ci} \\ u_{si} \\ v_i \\ \theta_i \\ u_{cj} \\ u_{sj} \\ v_j \\ \theta_j \end{Bmatrix} \tag{42}$$

or in compact form

$$\mathbf{u}_{pe} = \mathbf{T}_e\,\mathbf{d}_{pe} \tag{43}$$

where $\mathbf{u}_{pe}$ is the displacement vector of the tendon segment, $\mathbf{d}_{pe}$ collects the displacement vector of the two linked nodes and $\mathbf{T}_e$ is a transformation matrix which depends only on the undeformed coordinates of the segment end points. On the other hand, the displacements of the tendon segment can be related to the global displacement vector ($\boldsymbol{D}$) of the complete FE model by

$$\mathbf{d}_{pe} = \mathbf{L}_e\,\mathbf{D} \tag{44}$$

where $\mathbf{L}_e$ is a kinematic relation matrix relating the tendon d.o.f.'s segment $e$ with the global d.o.f.'s. Thus, the segment displacements can be directly related to the global displacements:

$$\mathbf{u}_{pe} = \mathbf{T}_e\,\mathbf{L}_e\,\mathbf{D} \tag{45}$$

As the strain is assumed constant along the tendon length, the internal virtual work associated with its deformation is given by:

$$\delta U_p = \int_{L_p} \int_{A_p} \delta\varepsilon_p\,\sigma_p\,\mathrm{d}A\,\mathrm{d}S = \delta\varepsilon_p\,F_p\,L_p \tag{46}$$

where $F_p = A_p\sigma_p$ is the tendon force and $L_p$ is the initial ($\boldsymbol{D} = \mathbf{0}$) tendon length. The tendon strain is given by the sum of a constant initial strain $\varepsilon_{p0}$ and the incremental displacement-dependent strain ($\Delta\varepsilon_p$):

$$\varepsilon_p = \varepsilon_{p0} + \Delta\varepsilon_p \tag{47}$$

The initial strain $\varepsilon_{p0}$ corresponds to a reference strain value yet to be defined. The incremental strain is defined as the engineering strain, leading to the following definition of total strain:

$$\varepsilon_p = \varepsilon_{p0} + \frac{\ell_p - L_p}{L_p} = \varepsilon_{p0} + \frac{\sum_{e=1}^{n_p}(\ell_{pe} - L_{pe})}{\sum_{e=1}^{n_p} L_{pe}} \tag{48}$$

where $L_{pe}$ and $\ell_{pe}$ are the initial and deformed segment lengths, and $n_p$ is the number of tendon segments.

The strain variation used in the evaluation of the virtual work can be obtained from the previous equation as

$$\delta\varepsilon_p = \frac{\delta\ell_p}{L_p} \tag{49}$$

The variation of a segment length can be written as:

$$\delta\ell_{pe} = \cos\beta\ (\delta u_{pj} - \delta u_{pi}) + \sin\beta\ (\delta v_{pj} - \delta v_{pi}) \tag{50}$$

where $\beta$ is the angle of the deformed segment with the horizontal axis. This equation can be conveniently cast in matrix form as

$$\delta\ell_{pe} = \begin{bmatrix} -\cos\beta & -\sin\beta & \cos\beta & \sin\beta \end{bmatrix} \begin{bmatrix} \delta u_{pi} \\ \delta v_{pi} \\ \delta u_{pj} \\ \delta u_{pj} \end{bmatrix} = \mathbf{r}_e^T\,\delta\mathbf{u}_{pe} \tag{51}$$

where $\delta\mathbf{u}_{pe}$ are the virtual displacements of the tendon segment. Summing up the contributions for all the elements which form the tendon yields the variation of the current length:

$$\delta\ell_p = \sum_{e=1}^{n_p} \delta\ell_{pe} = \sum_{e=1}^{n_p} \mathbf{r}_e^T\,\mathbf{T}_e\,\delta\mathbf{d}_{pe} \tag{52}$$

Therefore, the internal virtual work of the prestressing tendon is given by

$$\delta U_p = \delta\ell_p\,F_p = \sum_{e=1}^{n_p} \delta\ell_{pe}\,F_p = \sum_{e=1}^{n_p} \mathbf{r}_e^T\,\mathbf{T}_e\,\delta\mathbf{d}_{pe}\,F_p \tag{53}$$

This equation can be written in a compact form as

$$\delta U_p = \sum_{e=1}^{n_p} \mathbf{g}_{pe}^T\,\delta\mathbf{d}_{pe} \tag{54}$$

where the internal force vector of the each tendon segment is

$$\mathbf{g}_{pe} = \mathbf{T}_e^T \mathbf{r}_e F_p \tag{55}$$

or

$$\mathbf{g}_{pe} = \mathbf{w}_e F_p = \begin{bmatrix} -\cos\beta & -\sin\beta & e_i\cos\beta & \cos\beta & \sin\beta & -e_j\cos\beta \end{bmatrix}^T F_p \tag{56}$$

where $\mathbf{w}_e = \mathbf{T}_e^T \mathbf{r}_e$. It is important to note that, in Eq.(55), vector $\mathbf{r}_e$ depends only on the segment displacements $\mathbf{d}_{pe}$, while the tendon force $F_p$ depends on the global displacement vector $\mathbf{D}$.

Using Eq.(44), the tendon contribution to the global internal force is given by

$$\mathbf{g}_p = \sum_{e=1}^{n_p} \mathbf{L}_e^T \mathbf{g}_{pe} \tag{57}$$

In the actual computer implementation, the global internal force vector of the prestressing tendon can be obtained using the classical finite element assemblage operator:

$$\mathbf{g}_p = \mathop{\mathbf{A}}_{e=1}^{n_p} \left(\mathbf{g}_{pe}\right) \tag{58}$$

The tendon global tangent stiffness $\mathbf{K}_{Tp}$ is obtained straightforwardly from the differentiation of the global internal force vector with respect to the nodal displacements:

$$\mathbf{K}_{Tp} = \frac{\partial \mathbf{g}_p}{\partial \mathbf{D}} = \sum_{e=1}^{n_p} \mathbf{L}_e^T \frac{\partial \mathbf{g}_{pe}}{\partial \mathbf{D}} \tag{59}$$

Differentiating Eq.(55) with respect to the nodal displacements, one gets

$$\frac{\partial \mathbf{g}_{pe}}{\partial \mathbf{D}} = \mathbf{T}_e^T \frac{\partial \mathbf{r}_e}{\partial \mathbf{D}} F_p + \mathbf{T}_e^T \mathbf{r}_e \frac{\partial F_p}{\partial \mathbf{D}} \tag{60}$$

Therefore, the tangent stiffness matrix of the tendon is given by

$$\mathbf{K}_{Tp} = \sum_{e=1}^{n_p} \left( \mathbf{L}_e^T \mathbf{T}_e^T \frac{\partial \mathbf{r}_e}{\partial \mathbf{D}} F_p + \mathbf{L}_e^T \mathbf{T}_e^T \mathbf{r}_e \frac{\partial F_p}{\partial \mathbf{D}} \right) \tag{61}$$

The second term of the r.h.s. can be identified as the material stiffness matrix. The tendon force derivative with respect to the nodal displacements is given by

$$\frac{\partial F_p}{\partial \mathbf{D}} = A_p \frac{\partial \sigma_p}{\partial \varepsilon_p} \frac{\partial \varepsilon_p}{\partial \mathbf{D}} = \frac{A_p E_{pt}}{L_p} \sum_{a=1}^{n_p} \mathbf{r}_a^T \mathbf{T}_a \mathbf{L}_a \tag{62}$$

where the index $a$ was introduced because the tendon force $F_p$ depends on the displacements of the whole structure and not only on those of segment $e$ in Eq.(61). Therefore, the material stiffness matrix of the tendon can be written as

$$\mathbf{K}_{Ep} = \left( \frac{E_{pt} A_p}{L_p} \right) \mathbf{w}\mathbf{w}^T \tag{63}$$

where

$$\mathbf{w} = \sum_{e=1}^{n_p} \mathbf{L}_e^T \mathbf{w}_e = \mathop{\mathbf{A}}_{e=1}^{n_p} (\mathbf{w}_e) \tag{64}$$

Thus, $\mathbf{K}_{Ep}$ is a symmetric matrix whose dimension depends on the tendon discretization, since it connects only the degrees of freedom of the segment end nodes.

The first term of the r.h.s. of Eq.(60) corresponds to the geometric stiffness matrix of the tendon segment. The derivative of the vector $\mathbf{r}_e$ with respect to the global displacement vector is given by

$$\frac{\partial \mathbf{r}_e}{\partial \mathbf{D}} = \frac{\partial \mathbf{r}_e}{\partial \mathbf{d}_{pe}} \frac{\partial \mathbf{u}_e}{\partial \mathbf{D}} = \frac{\partial \mathbf{r}_e}{\partial \mathbf{d}_{pe}} \mathbf{L}_e \tag{65}$$

where the derivative of $\mathbf{r}_e$ with respect to $\mathbf{d}_{pe}$ is given by

$$\frac{\partial \mathbf{r}_e}{\partial \mathbf{u}_{pe}} = \frac{\partial \mathbf{r}_e}{\partial \beta} \frac{\partial \beta}{\partial \mathbf{u}_{pe}} \frac{\partial \mathbf{u}_{pe}}{\partial \mathbf{d}_{pe}} = \mathbf{z}_e \frac{\partial \beta}{\partial \mathbf{u}_{pe}} \mathbf{T}_e \tag{66}$$

with

$$\mathbf{z}_e^T = \begin{bmatrix} \sin\beta & -\cos\beta & -\sin\beta & \cos\beta \end{bmatrix} \tag{67}$$

and

$$\frac{\partial \beta}{\partial \mathbf{u}_{pe}} = \frac{\mathbf{z}_e^T}{\ell_{pe}} \tag{68}$$

The geometric stiffness matrix of the tendon is then given by

$$\mathbf{K}_{Gp} = \sum_{e=1}^{n_p} \mathbf{L}_e^T \mathbf{K}_{Gp_e} \mathbf{L}_e = \mathop{\mathbf{A}}_{e=1}^{n_p} \left(\mathbf{K}_{Gp_e}\right) \tag{69}$$

where

$$\mathbf{K}_{Gp_e} = \left( \frac{F_p}{\ell_{pe}} \right) \mathbf{T}_e^T \mathbf{z}_e \mathbf{z}_e^T \mathbf{T}_e \tag{70}$$

corresponds to the geometric stiffness matrix of a tendon segment. According to the above expressions the geometric stiffness is a sparse symmetric matrix with the same sparsity pattern than the stiffness matrix of the embedding beam.

Finally, the tangent stiffness matrix of the prestressing tendon is the sum of the material and geometric stiffness matrices:

$$\mathbf{K}_{Tp} = \mathbf{K}_{Ep} + \mathbf{K}_{Gp} \tag{71}$$

## 5. Prestressing step simulation

In this work, the post-tensioning operation is assumed to be carried out in a single step by means of devices such as hydraulic jacks, on either one or both ends of the prestressing tendon. No friction loss is assumed at the deviators, so that the tendon is under a constant state of stress and strain.

The main difficulty on the numerical modeling of the post-tensioning operation is the lack of compatibility between the tendon

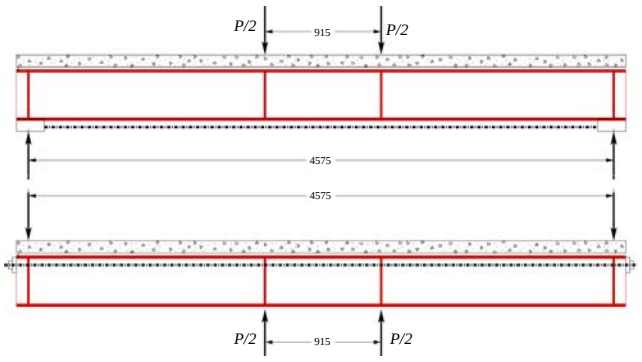


**Fig. 3.** Prestressed composite beams—positive and negative bending.

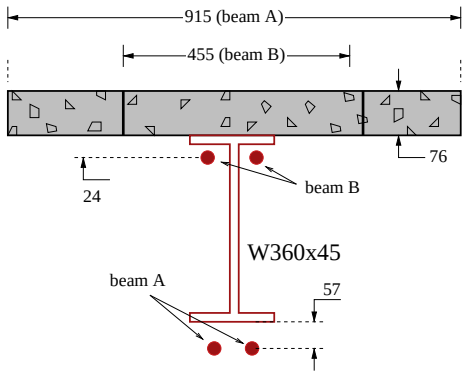


**Fig. 4.** Cross sections for positive (beam A)and negative (beam B)bending.

and the composite beam, which makes difficult to trace the material points of the former.

It is usual that the only information available is the final value of tendon stress. In the present work, the procedure developed in [18] will be adapted for the PSCCB post-tensioning step. The procedure relies on the observation that after the post-tensioning is finished and the ends of the tendon are anchored, there is a displacement field $\mathbf{u}$ for the mesh of beam and tendon which is in equilibrium with the forces applied by the tendon at anchorage and deviator points. These forces depend on the tendon final force $F_{pe} = A_p\sigma_{pe}$ and associated strain $\varepsilon_{pe}$.

A similar, but not completely equivalent, situation consists in the positioning of a pretensioned tendon with initial stress $\sigma_{p0}$, related to a strain $\varepsilon_{p0}$, fixed on the same points (anchorages and deviators) of the undeformed beam. Upon release, the system will eventually reach a state of equilibrium with a displacement field $\mathbf{u}$, which will change the strain $\varepsilon_{p0}$ and stress $\sigma_{p0}$ states of the tendon. The nonlinear equilibrium system to be solved is

$$\mathbf{g}(\mathbf{u}) = \mathbf{g}_b + \mathbf{g}_p = \mathbf{0} \tag{72}$$

where the tendon state is given by

$$\varepsilon_p = \varepsilon_{p0} + \Delta\varepsilon_p(\mathbf{u}) \tag{73}$$

$$\sigma_p = \sigma_{p0} + \Delta\sigma_p\left(\Delta\varepsilon_p(\mathbf{u})\right) \tag{74}$$

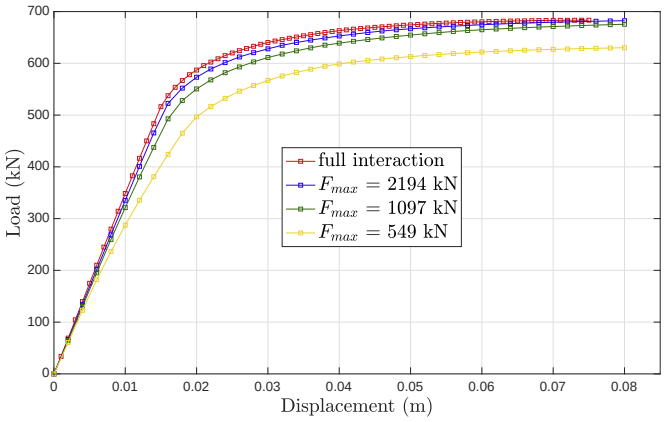


**Fig. 6.** Load-displacement for beam A [1] with different connections.

It is clear by similarity that if the final stress of this system is equal to the desired value $\sigma_{pe}$, leading to a final force $F_{pe}$, the correct values of displacement for the prestressing step are obtained. Therefore the initial problem is reduced to finding which value of initial strain $\varepsilon_{p0}$ will produce $F_p = F_{pe}$. This could be done by a one-dimensional search procedure such as bissection of interval.

Another option is to explicitly construct a system of nonlinear equations, where all the conditions are simultaneously met:

$$\hat{\mathbf{r}} = \begin{bmatrix} \mathbf{g}(\mathbf{u}, \varepsilon_{p0}) \\ F_p(\mathbf{u}, \varepsilon_{p0}) - F_{pe} \end{bmatrix} = [\mathbf{0}\,0] \tag{75}$$

This nonlinear system can be solved using the Newton-Raphson method and may be interpreted as a variant of the usual path-following methods in which the step is strain-controlled. Upon linearization one gets

$$\begin{aligned} &\mathbf{g} + \frac{\partial \mathbf{g}}{\partial \mathbf{u}}\delta\mathbf{u} + \frac{\partial \mathbf{g}}{\partial \varepsilon_{p0}}\delta\varepsilon_{p0} = 0 \\ &F_p - F_{pe} + \frac{\partial F_p}{\partial \mathbf{u}}\delta\mathbf{u} + \frac{\partial F_p}{\partial \varepsilon_{p0}}\delta\varepsilon_{p0} = 0 \end{aligned} \tag{76}$$

where $i$ is the iteration number and $\delta\mathbf{u}$ and $\delta\varepsilon_{p0}$ are the iterative

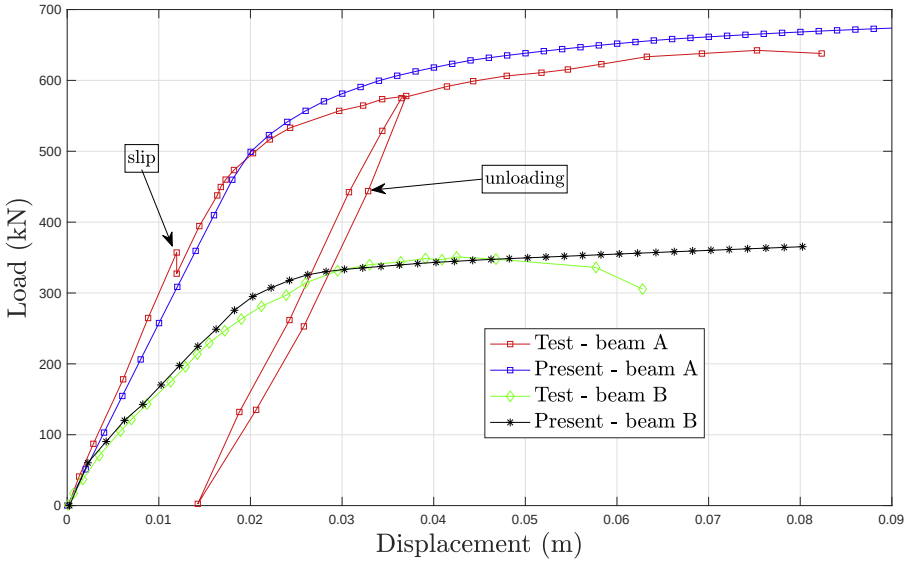


**Fig. 5.** Load-displacement for beams A and B from Saadatmanesh et al. [1].

**Table 1**
Peak load comparison [1].

| Beam | Test | Numerical | Error |
|---|---|---|---|
| A | 642 | 674 | 4.98% |
| B | 351 | 365 | 3.99% |

corrections. The internal force of the structure is given by

$$\mathbf{g} = \mathbf{g}_b + \mathbf{g}_p = \mathbf{g}_b + F_p \mathbf{w} \tag{77}$$

Since the internal force vector of the beam elements ($\mathbf{g}_b$) is considered independent on the initial prestressing strain $\varepsilon_{p0}$:

$$\frac{\partial \mathbf{g}}{\partial \varepsilon_{p0}} = \frac{\partial F_p}{\partial \varepsilon_{p0}} \mathbf{w} = A_p \frac{\partial \sigma_p}{\partial \varepsilon_p} \frac{\partial \varepsilon_p}{\partial \varepsilon_{p0}} \mathbf{w} = A_p E_{pt} \mathbf{w} \tag{78}$$

In addition, using Eq.(62):

$$\frac{\partial F_p}{\partial \mathbf{u}} = A_p \frac{\partial \sigma_p}{\partial \varepsilon_p} \frac{\partial \varepsilon_p}{\partial \mathbf{u}} = \frac{A_p E_{pt}}{L_p} \mathbf{w}^T \tag{79}$$

Therefore, Eq.(76) can be written as

$$\begin{cases} \mathbf{K}_T \delta \mathbf{u} + \delta \varepsilon_{p0} A_p E_{pt} \mathbf{w} = -\mathbf{g} \\ \dfrac{A_p E_{pt}}{L_p} \mathbf{w}^T \delta \mathbf{u} + A_p E_{pt} \delta \varepsilon_{p0} = F_{pe} - F_p \end{cases} \tag{80}$$

In order to efficiently solve this system, the displacement increment is written as

$$\delta \mathbf{u} = \delta \mathbf{u}_1 + \delta \varepsilon_{p0} \delta \mathbf{u}_2 \tag{81}$$

where

$$\begin{cases} \mathbf{K}_T \delta \mathbf{u}_1 = -\mathbf{g} \\ \mathbf{K}_T \delta \mathbf{u}_2 = -A_p E_{pt} \mathbf{w} \end{cases} \tag{82}$$

The substitution of Eq.(81) in the second line of Eq.(80) yields the strain increment:

$$\delta \varepsilon_{p0} = \frac{(F_{pe} - F_p) L_p - A_p E_{pt} \mathbf{w}^T \delta \mathbf{u}_1}{A_p E_{pt} (\mathbf{w}^T \delta \mathbf{u}_2 + L_p)} \tag{83}$$

Thus, the displacements and the initial prestressing strain are updated in each iteration as

$$\begin{aligned} \mathbf{u}_{i+1} &= \mathbf{u}_i + \delta \mathbf{u} \\ \varepsilon_{p0_{i+1}} &= \varepsilon_{p0_i} + \delta \varepsilon_{p0} \end{aligned} \tag{84}$$

where $\delta \mathbf{u}$ is computed using Eq.(81). This iterative procedure can be stopped when

$$\frac{\|\hat{\mathbf{r}}\|}{F_{pe}} \leq \text{TOL} \tag{85}$$

where TOL is the prescribed tolerance for convergence. This iterative procedure is very robust and converges in few steps, and may be initialized with $\mathbf{u} = \mathbf{0}$ and $\varepsilon_{p0} = 0$. Obviously the tendon strain is easily bounded to furnish an interval that contains the solution. After this step is complete the global displacement vector $\mathbf{D}$ is initialized with the displacement vector $\mathbf{u}$ and the load application phase is carried out, either with load or displacement control.

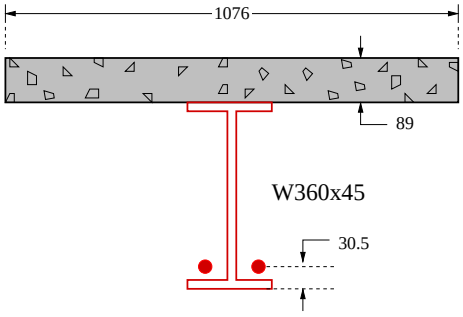


**Fig. 7.** Cross section at midspan for beams A, B and C from Ayyub et al. [2].

## 6. Applications

Examples of prestressed steel-composite beams were analyzed with the described procedure. Otherwise stated, in all the cases meshes with 18 elements were employed, and along the beam gauss integration with four points. At the cross section level, the fiber method is used with eight layers for the steel web, two layers for the flanges and eight layers for the concrete slab. To the knowledge of the authors, most experimental tests carried out so far employed designs of beams aiming at full interaction, as prescribed in design codes such as Eurocode 4. This implies a number of shear studs able to minimize the connection slip. The ocurrence of slip, even with full interaction design, was reported in some of these works, but a study on the influence of weaker shear connections still remains to be done.

In the numerical model the shear connection force-slip relation is based on the Ollgaard expression with a straight secant line for small values of $s$, and the individual connection ultimate force is evaluated with the expression

$$F_u = A_{cs} \frac{\sqrt{f_c E_c}}{2} \tag{86}$$

where $A_{cs}$ is the connector section, $f_c$ and $E_c$ the ultimate resistance and the elastic modulus of the concrete. This value is then smeared along the connection. The precision of this approach is hard to ensure, since the experimental results show a great influence of effects such as bond between steel and concrete. Nonetheless it is important to assess the effects of different connection properties on the overall beam behaviour.

### 6.1. Experiments by Saadatmanesh et al.(1989)

Saadatmanesh et al. [1] carried out tests with simply supported beams subjected to positive and negative bending moments and compared the results with those obtained from their analytical-numerical formulation [7]. In the latter, deflections, stresses, and strains were calculated with an incremental deformation method, ensuring compatibility of deformations and equilibrium of forces, without slip. Full interaction was also considered in the design of the connection for the tests. In the original work, the beams under positive and negative bending were identified as A and B respectively. Geometric data for both beams is shown in Fig. 3.

Beam A had a concrete with peak stresses of 33.4 MPa and 3 MPa in compression and tension respectively. Reinforcement consisted of 10 mm diameter deformed bars, three spaced longitudinally at 229 mm on centers and 11 transversely at 455 mm on centers. The longitudinal reinforcement had yield stress of 367 MPa, elastic modulus 200 GPa and hardening stiffness 3 GPa. The steel beam was prestressed with two 16 mm diameter Grade 150 DYWIDAG threadbars with 910 MPa and 1090 MPa yield and ultimate stresses respectively, reaching 98 kN, placed under the bottom flange of the beam. Pairs of 13-mm diameter by 51 mm long shear studs were welded to the top flange, 120 mm on centers, between the load points and the supports. The mean tensile properties of three test specimens cut from the web

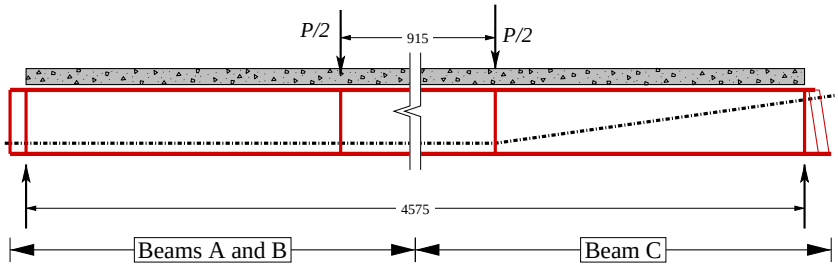


**Fig. 8.** Geometry of PSCCB with straight and draped tendon from [2].

of the beam were 367 MPa yield stress, 520 MPa tensile strength, and 24% elongation.

Beam B had a concrete with peak stress of 32.4 MPa in compression and 2.8 MPa in tension. The same shear studs were placed at 610 mm on centers between each load point and the nearby support. Reinforcement consisted of two 10-mm diameter deformed bars placed longitudinally at 152 mm on centers and ten transversely at 455 mm. The steel beam had 379 MPa yield strength and 530 MPa tensile strength, and 26% elongation.

The cross sections are shown in Fig. 4. both concrete slabs were 76 mm thick, and the widths are 915 mm and 455 mm for beams A and B respectively. Stiffeners were placed under the points of applied load for both beams.

In beam A, the steel beams are prestressed before the concrete was cast. This would prevent the comparison with the present model during prestressing. Nonetheless the comparison may be made with the displacements due to external loading only.

In the present numerical analysis the connection constitutive law was described by Eq.(40), with the parameters $\alpha$ and $\beta$ taken respectively as 0.588 and 1000 $mm^{-1}$. The maximum value of the connection force is obtained smearing the resistance of 16 single studs per meter, and the ultimate load of a single stud was established as 68.58 kN. Up to a slip of 0.1 mm a secant value is used for the load-slip relation. In the region between the loads, where there are no studs, a very small connection force is attributed to the elements to avoid numerical problems.

Fig. 5 shows the load-displacement curve for beams A and B, for the present numerical procedure, along with the experimental values, adapted from the original work.

With respect to the beam subject to positive moment, a very good agreement may be verified. The initial stiffness in the elastic portion is well represented by the numerical model. The ultimate load is higher for the present procedure, which might be due to the consideration of the whole section already working during the prestressing step, delaying the compressive forces on the concrete section.

In the experimental setup, no slip was observed until there was a loss of bond between the flange and the slab, with a load of 356 kN. After that there is a slight drop of the load and then a gradual loss of stiffness is observed. The tension flange extreme fiber yields at 445 kN and the ultimate load is attained as 641 kN, when the concrete crushes. During the test an unloading-reloading step was undertaken at 578 kN, as may be seen in the figure.

For beam B, which is subjected to pretensioning near the concrete slab, simulating a hogging moment region, once again the agreement between the results is quite good. The spacing of connectors equal to 610 mm is large, providing a weak shear connection. The tests showed a reduction of the load level after reaching the maximum value. The authors explained that this was due to local buckling of the lower flange, which the present numerical procedure is unable to catch.

The proposed procedure was employed to study the influence of the connection stiffness on the load-displacement pattern of beam A. A full interaction analysis based on the formulation by Moreira et al. [18] is compared with the above connection stiffness (based on 16 studs smeared along 1 m) and with weaker shear connections, even if these low values are not admissible by design codes. The results for the load-displacement behaviour in these cases are depicted in Fig. 6. There is a reasonable influence on the stiffness and strength of the beam with the variation on the connection stiffness.

Table 1 shows the comparison of the maximum loads in each situation along with the relative error.

For beam B (negative moment), increasing the connection stiffness (e.g. by reducing space between studs) has practically no effect on the behavior of the composite beam, therefore this comparison will not be shown here.

**Table 2**
Peak load comparison [2].

| Beam | Test | Numerical | Error |
|---|---|---|---|
| A | 709 | 716 | 0.98% |
| C | 773 | 762 | −1.42% |

### 6.2. Experiments by Ayyub et al. (1990)

The paper by Ayyub, Sohn and Saadatmanesh [2] presents tests with three externally prestressed simply supported composite beams (named A,B and C). Differences between the beams were on layout and type of prestressing component. Straight elements were used for beams A and B, and draped for beam C. Strands were used for beams B and C, while beam A was tensioned by a deformed bar. Details of the cross section and geometry are shown in Figs. 7 and 8 respectively.

The authors also employed a formulation based on the transformed area method and the strain compatibility method in their analyses. The ultimate capacity was calculated by assuming fully plastic state of the

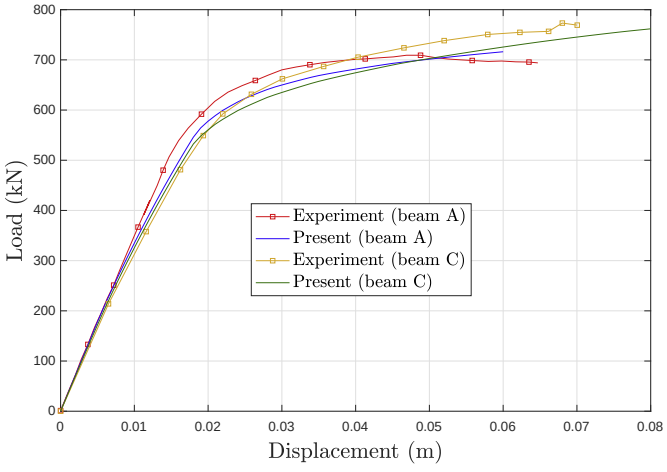


**Fig. 9.** Load-displacement curves for beams A and C from Ayyub et al. [2].

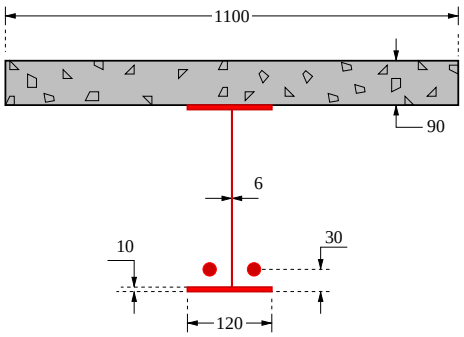


**Fig. 10.** Section of beam BS2 [3].

cross section. End rotations and deflection at midspan were obtained by integrating the curvature along the span.

In the present work, beams A and C will be analyzed, as A and B displayed a very similar behavior. For beam A, a W360 × 45 rolled steel beam 4.83 m long was supported on a 4.57 m simple span. The 1.07 m wide, 90 mm thick, and 4.73 m long concrete slab was connected to the steel beam by stud connectors. Pairs of 16 mm diameter stud connectors, spaced by 93 mm, were placed along the shear spans, except between the applied loads. Reinforcement consisted of 9.5 mm diameter Grade 60 (yield stress 414 MPa) deformed bars placed in two orthogonal directions. Straight 16 mm prestressed threadbars were placed 30.5 mm above the bottom part of the lower flange. The bars were extended on both sides of the web along the full length of the beam. The prestressing was performed before the concrete was cast to prevent the tensile cracking. Four pairs of stiffeners are present on deviator and anchorage points.

Beam C is identical except for the draped tendon profile, and the use of strands for prestressing. The inclined portion of the draped tendon was placed at an angle of 9.2 degrees with the beam axis. The strands were anchored at both ends, 32 mm below the top (compression) flange and were positioned between loading points 30.5 mm above the bottom (tension) flange. Cross sections are identical as well as the overall design.

The adopted material properties are as follows: for the concrete, the peak compressive stress is 40 MPa, and the tensile stress 4 MPa. For the steel of the beams, the yield stress is 411,6 MPa with elastic modulus 200 GPa. For the prestressing strands, the stress $f_{yp}$ is taken as 1620 MPa and elastic modulus $E_p$ is 195 MPa. For the prestressing bar, yield strength $f_{yp}$ is taken as 915 MPa. The tendon forces are 267 kN for both beams.

In the present numerical analysis the same parameters of the previous example are used to describe the connection load-slip relation, but the smaller spacing results in a higher value of the connection peak resistance. A single connector is assumed to have maximum load of 42.2 kN (Table 2).

Results for the vertical displacement of the central section of the beams are shown in Fig. 9, along with the experimental measurements. There is a very good correspondence between the numerical and experimental results.

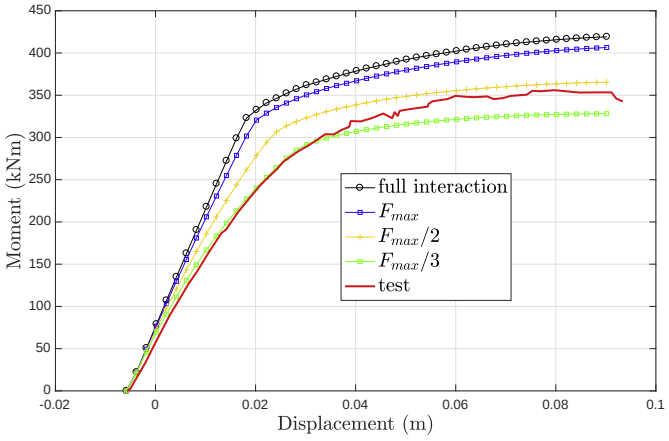


**Fig. 12.** Moment-displacement results for beam BS2 [3].

### 6.3. Tests by Chen and Gu (1990)

For another verification of the proposed model the prestressed composite beam, designated BS2, from the work of Chen and Gu [3] was selected. The beam was prestressed with straight external tendons with no deviators along the span, placed at 30 mm above the bottom of beam. The tendons consisted of two 7$\phi$5 high-strength steel strands with cross section of 137.4 mm$^2$, and the initial prestress was 819.5 MPa. Two rows of 16 mm diameter by 65 mm long shear studs were welded to the top flange with a transverse spacing of 76 mm symmetric to the centerline of the top flange and a longitudinal spacing of 200 mm. Details of the beam section and geometry are shown in Figs. 10 and 11.

The material properties are as follows: for the concrete, the peak stress $f_c$ is 41 MPa; for the profile steel, the yield stress is 327,7 MPa and 406,5 MPa for the web and flange respectively, with elastic modulus 200 GPa; for the prestressing steel, the plastic stress is $f_{yp}$ is taken as 1860 MPa and elastic modulus $E_p$ is 195 MPa. Although the beams were designed for full interaction, slip was measured at the ends: for BS1 the maximum slips during the test were 0.4 and 0.5 mm, and for BS2 they were 0.6 and 0.5 mm. A 3D FE model was used to assess the results with good agreement. The authors also presented an analytical method, based on rigid plastic assumptions, for the evaluation of the ultimate capacity of the beams and the tendon force increment, for different layouts of tendons. The authors presented the results in terms of external bending moment rather than applied loads, which requires the evaluation of the total bending effects at midspan. The values of total moment from the original work apparently include the weight of the beam and the experimental apparatus, but were not taken into account in the present work.

Based on the description of the shear stud connection, the average number of shear connectors per unit length is initially taken as 10 (2 rows of studs at 200 mm spacing) and the correspondent value of ultimate force is adopted for the force-slip relation, with the same parameters $\beta$ and $\alpha$ from the previous examples. This resulted in a higher

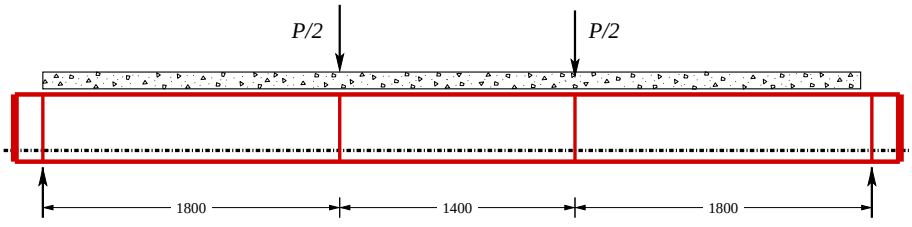


**Fig. 11.** Geometry of beam BS2 [3].

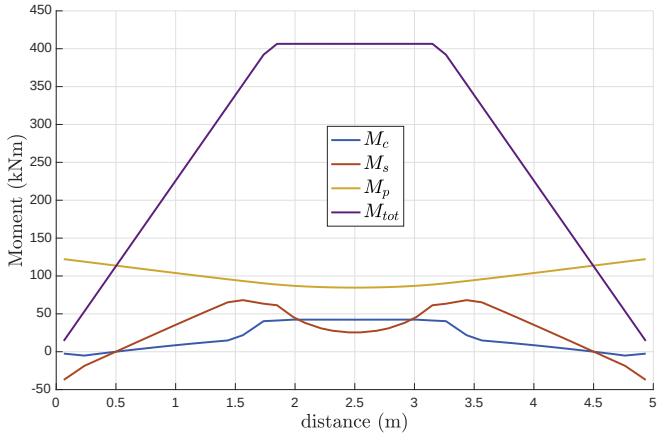


**Fig. 13.** Bending moment components results for beam BS2.

moment capacity for the beam when compared to the experimental results. In their FE analyses, Chen and Gu [3] used spring-link elements to simulate the connection, but did not provide the value of the connection strength or stiffness. Therefore, different values of the connection stiffness, including a full-interaction analysis, and the corresponding results for the moment-displacement curves are depicted in Fig. 12. It is clear from the results that this PSCCB is very sensitive to changes on the properties of the shear connection. It is worth noting that beam BS2 has no intermediate fixed points (deviators). The geometric nonlinearity then plays an important role as the eccentricity of the tendon varies due to the vertical displacement.

It is interesting to visualize the different components of the total bending moment and their distribution along the beam length. Fig. 13 shows the variations of $M_c$, $M_c$, internal bending moments of the concrete and steel section, and $M_p$, the contribution to internal bending moment of the tendon, which is given by

$$M_p = F_p\left(h - e_p(x) + v(x)\right) \tag{87}$$

where $h$ is the distance between the reference axes of the two sections, $e_p(x)$ is the tendon eccentricity and v(x) the transverse displacement of the beam. The total moment taken with respect of the concrete axis is the sum of the following components

$$M_{tot} = M_c + M_s + N_s h + F_p\left(h - e_p(x) + v(x)\right) \tag{88}$$

where $N_s$ is the normal force on the steel section. This moment counteracts the external moment which is readily available.

### 6.4. Beams tested by Lorenc and Kubica (2006)

Lorenc and Kubica [6] presented in 2006 a large set of experimental results for six simply supported composite steel–concrete beams, five of which post-tensioned, one non-prestressed. The beams were subjected to positive bending until failure. Straight and draped tendons were used. The influence of shear connection flexibility was taken into account and slip was measured along the beam axis. Additionally, force-slip relations for the connections were determined by test of push-out specimens. The geometric characteristics of the 6 beams are depicted in Fig. 14, where the difference between the draped and straight tendon layouts is shown. The cross section for the beams is shown in Fig. 15.

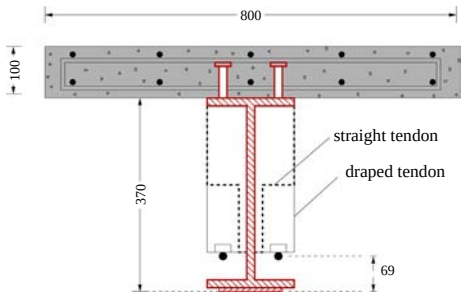


**Fig. 15.** Prestressed composite beam cross section from [6].

Each beam consisted of an unpropped steel profile IPE360 with a 4500 mm long coverplate and an 800 mm wide and 100 mm thick concrete slab. Shear connectors (KB 13×75 mm, S235J2G3 + C450) were spaced at every 100 mm along the whole length of the beam, except for 50 cm close to the support regions where studs were placed in three rows at a spacing of 80 mm. Force-slip relations for the connections, based on push-out tests and employed in the theoretical analysis of the authors, led to the definition of the Ollgaard general equation with parameters $\alpha$ 0.3 and $\beta$ 0.550 mm$^{-1}$. The maximum force of a single connector was established as 75 kN.

Deviator plates of the draped tendons are cut in the case of straight tendon. The six composite beams tested are named B1, B3 and B5 (draped tendons), B4 and B6 (straight tendons), and B2 (non-prestressed). Load-midspan displacements, tendon stresses, strains on top and coverplate bottoms were presented for all beams. More detailed experimental results including slips were given for B3, B4 and B6 specimens. Seven-wire strands with a nominal diameter of 15.7 mm, a cross-sectional area of 150 mm$^2$ and a tensile strength of 1860 MPa were used. The strand modulus of elasticity $E_s$ was 197.8 GPa. The slabs had two different concretes: CI (weaker) and CII (stronger). Initial values of concrete peak stress were obtained from cylinders 150 × 300 mm, and from smaller specimens cut out from the beams after the tests.

In this paper beams B3 (draped) and B6 (straight) were analyzed by the numerical procedure. The load-displacement curves of the five prestressed beams presented in the original work are very close to each other, except beam B4 which according to visual inspection prior to testing showed the slab concrete to be damaged in some points and with shrinkage cracks. Beam B3 has a total pretensioning force of 281 kN, while B6 was prestressed with a total force of 300 kN. The individual strengths of the stud bolts were evaluated by Eq.(86). Concrete strength is taken as the average of the cylinder values.

Fig. 16 depicts the load-midspan displacement behavior of beam B3, showing good agreement between the experimental values and the present formulation.

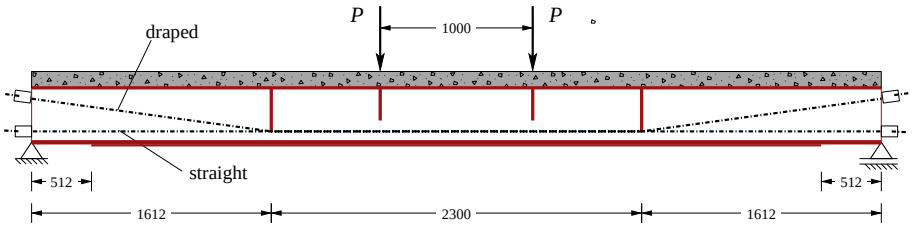


**Fig. 14.** Prestressed composite beam geometry from [6].

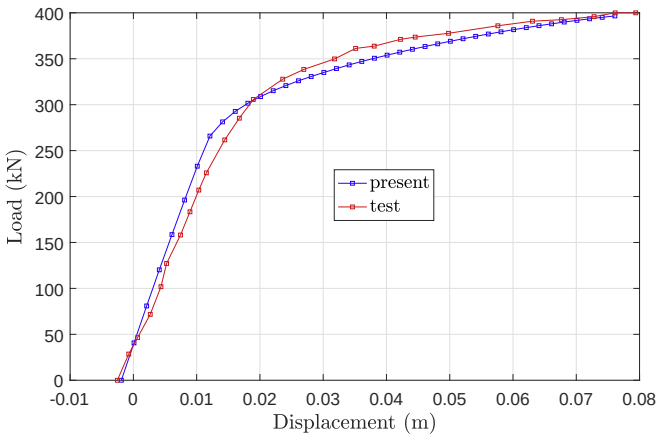


**Fig. 16.** Midspan displacement for beam B3.

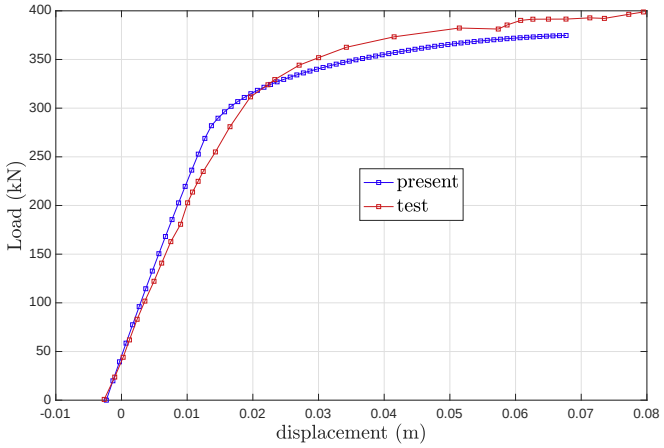


**Fig. 18.** Midspan displacement for beam B6.

In the original work, experimental results of axial strains along beam B3 were given for 4 load levels (0 kN-after prestressing, 200, 300 and 360 kN) in seven discrete points along the span. Fig. 17 compares the values of axial strain measured and calculated on the top of the concrete slab ($\varepsilon_c$) and on the bottom of the steel coverplate ($\varepsilon_s$). A very good agreement with the discrete experimental results is observed, except at midspan for the maximum load, after there has been yielding and large variations on measured strains are expected.

The load-midspan displacement curve for beam B6 is shown in Fig. 18. Once again a good agreement was obtained and the overall stiffness and load carrying capacity as predicted by the numerical model are close to the experimental values.

Fig. 19 shows the comparison between the strains on top of the concrete slab and the coverplate bottom for beam B6. In this case the value of the maximum strain in the coverplate flange was extrapolated for the original data. As may be seen from the pattern of the steel and concrete strains the region between the applied loads does not have a constant value even though external moment is constant. The reason is the influence of the tendon geometric nonlinear effect which alters the distribution of moment components in the central region of the beam.

The authors reported that in all the beams, including the non-prestressed one, the slab failed at the ends, cracking over the studs, under force $P$ of 250–300 kN. As the load was increased, the cracks propagated in the slab's bottom obliquely towards midspan. This effect obviously is not detectable by the present FE model. They also detected a large influence of adherence on the behavior of the composite steel-concrete connection. The value of the shear force per stud at cohesion breakdown was close to the value of the design shear resistance of a single stud connector. Therefore, there was no flexible connection up to the yield load.

The value of the ultimate load for the two beams analyzed is compared with the test values in Table 3.

## 7. Summary and conclusions

Prestressed steel-concrete composite beams are an efficient solution with greater load-carrying capacity and improved overall behaviour with respect to their non-prestressed counterparts. Few works, however, have considered the partial interaction or connection flexibility in the context of PSCCBs. This paper presented a nonlinear displacement-based FE formulation for PSCCBs, comprising beam and tendon elements, where the tendon is considered as a load-resisting member, and the relative displacements between steel and concrete (partial interaction) may be taken into account. The numerical analysis of the prestressing step is carried out by the adaptation of a newly develped strain-controlled equilibrium procedure, followed by a displacement controlled load stage. A very good agreement was observed between the proposed numerical model and experiments from various authors. The examples showed, for instance, the influence of the consideration of the partial interaction for the correct simulation of the PSCCB both in terms of stiffness and ultimate resistance, and the importance of the tendon nonlinear geometric effects on the distribution of moments and strains along the members. It is important to note that the design of

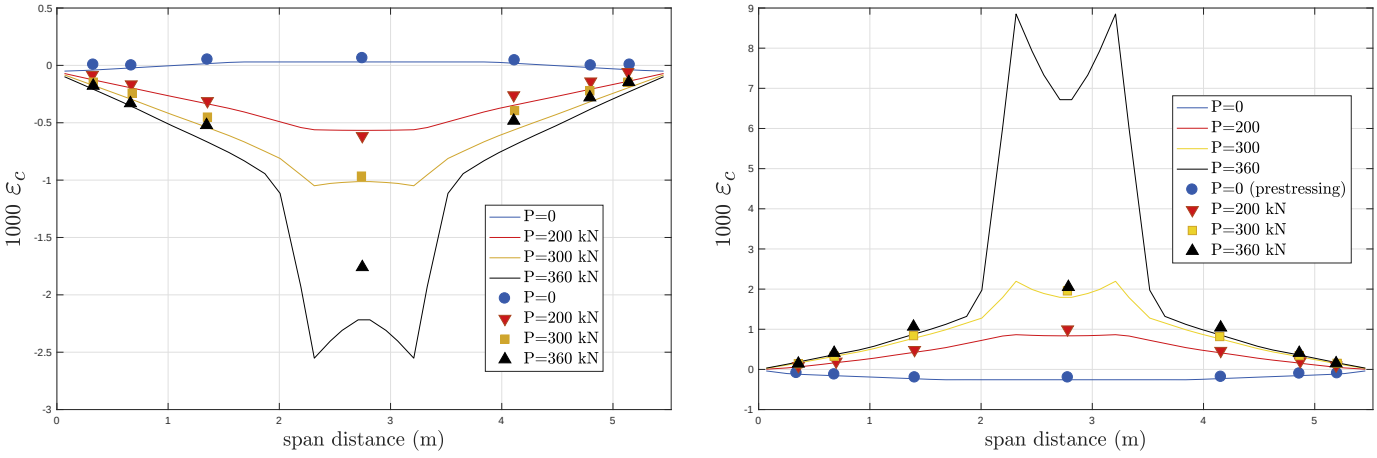


**Fig. 17.** Strains on concrete and steel fibers for beam B3.

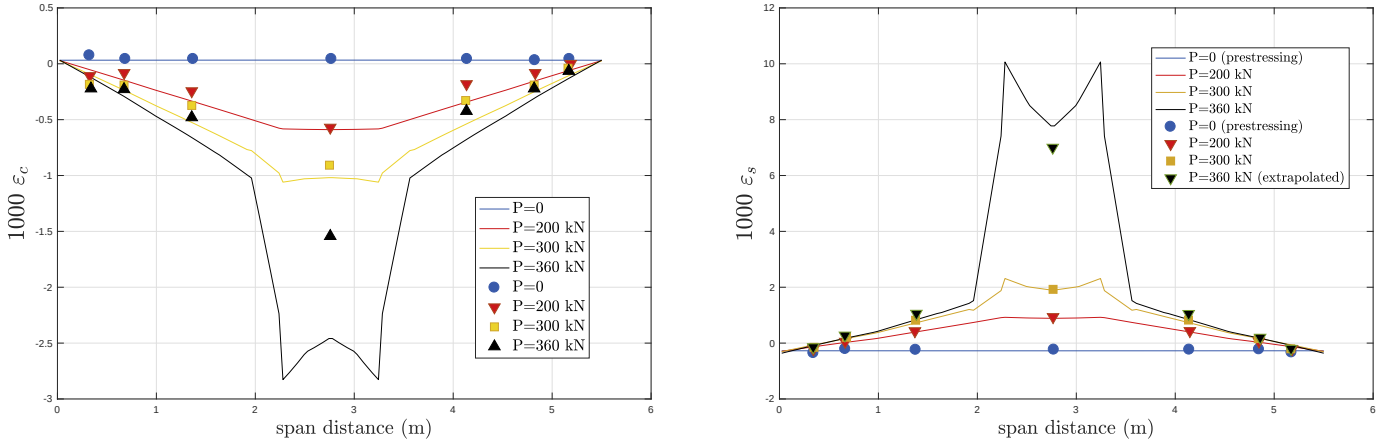


**Fig. 19.** Strains on concrete and steel fibers for beam B6.

**Table 3**
Peak load comparison [6].

| Beam | Test | Numerical | Error |
|---|---|---|---|
| B3 | 404 | 382 | −5.44% |
| B6 | 396 | 375 | −5.30% |

the experiments was done with the objective of attaining full interaction of the connection, with small values of slip measured during the tests. Further research is necessary to obtain load-slip relations which characterize more precisely the behavior of the steel-concrete interface and may include, for instance, the important effect of bond between steel and concrete. The proposed procedure constitutes a reliable, robust and computationally inexpensive option for the assessment of post-tensioned steel-concrete beams.

## Acknowledgements

The authors wish to thank CNPq (Conselho Nacional de Desenvolvimento Científico e Tecnológico, grants 307643/2016-6, 307616/2017-7), CAPES (Coordenação de Aperfeiçoamento de Pessoal de Nível Superior) and FUNCAP (Fundação Cearense de Amparo à Pesquisa) for the financial support to this work.

## References

[1] H. Saadatmanesh, P. Albrecht, B.M. Ayyub, Experimental study of prestressed composite beams, J. Struct. Eng. 115 (9) (1989) 2348–2363, https://doi.org/10.1061/(ASCE)0733-9445(1989)115:9(2348).
[2] B.M. Ayyub, Y.G. Sohn, H. Saadatmanesh, Prestressed composite girders under positive moment, J. Struct. Eng. 116 (11) (1990) 2931–2951, https://doi.org/10.1061/(ASCE)0733-9445(1990)116:11(2931).
[3] S. Chen, P. Gu, Load carrying capacity of composite beams prestressed with external tendons under positive moment, J. Constr. Steel Res. 61 (4) (2005) 515–530, https://doi.org/10.1016/j.jcsr.2004.09.004.
[4] A. El-Zohairy, H. Salim, A. Saucier, Steel-concrete composite beams strengthened with externally post-tensioned tendons under fatigue, J. Bridg. Eng. 24 (5) (2019), 04019027. https://doi.org/10.1061/(ASCE)BE.1943-5592.0001390.
[5] G. Bertagnoli, D. Gino, E. Martinelli, Prestressing of simply supported composite bridges: a cost-benefit analysis, in: J. Marcinowski (Ed.), XIII International Conference on Metal Structures (ICMS2016), Zielona Gora, CRC Press, Poland 2016, pp. 149–158.
[6] W. Lorenc, E. Kubica, Behavior of composite beams prestressed with external tendons: experimental study, J. Constr. Steel Res. 62 (12) (2006) 1353–1366, https://doi.org/10.1016/j.jcsr.2006.01.007.
[7] H. Saadatmanesh, P. Albrecht, B.M. Ayyub, Analytical study of prestressed composite beams, J. Struct. Eng. 115 (9) (1989) 2364–2381, https://doi.org/10.1061/(ASCE)0733-9445(1989)115:9(2364).
[8] J. Nie, M. Tao, C.S. Cai, S. Li, Analytical and numerical modeling of prestressed continuous steel-concrete composite beams, J. Struct. Eng. 137 (12) (2011) 1405–1418, https://doi.org/10.1061/(ASCE)ST.1943-541X.0000409.
[9] G. Bertagnoli, D. Gino, E. Martinelli, A simplified method for predicting early-age stresses in slabs of steel-concrete composite beams in partial interaction, Eng. Struct. 140 (2017) 286–297, https://doi.org/10.1016/j.engstruct.2017.02.058.
[10] A. Dall'Asta, L. Dezi, Nonlinear behavior of externally prestressed composite beams: analytical model, J. Struct. Eng. 124 (5) (1998) 588–597, https://doi.org/10.1061/(ASCE)0733-9445(1998)124:5(588.
[11] A. Dall'Asta, A. Zona, Finite element model for externally prestressed composite beams with deformable connection, J. Struct. Eng. 131 (5) (2005) 706–714, https://doi.org/10.1061/(ASCE)0733-9445(2005)131:5(706).
[12] A. Dall'Asta, L. Ragni, A. Zona, Analytical model for geometric and material nonlinear analysis of externally prestressed beams, J. Eng. Mech. 133 (1) (2007) 117–121, https://doi.org/10.1061/(ASCE)0733-9399(2007)133:1(117.
[13] A. Zona, L. Ragni, A. Dall'Asta, Finite element formulation for geometric and material nonlinear analysis of beams prestressed with external slipping tendons, Finite Elem. Anal. Des. 44 (15) (2008) 910–919, https://doi.org/10.1016/j.finel.2008.06.005.
[14] T. Lou, S. Lopes, A. Lopes, Numerical modeling of externally prestressed steel-concrete composite beams, J. Constr. Steel Res. 121 (2016) 229–236, https://doi.org/10.1016/j.jcsr.2016.02.008.
[15] S. Mohamed, A.B. Abu-Sena, I.G. Shaaban, K.A.A.M. Gharib, Effect of geometrical properties on strength of externally prestressed steel–concrete composite beams, Proceedings of the Institution of Civil Engineers – Structures and Buildings, 2018, https://doi.org/10.1680/jstbu.17.00172, avilable online.
[16] A. El-Zohairy, H. Salim, H. Shaaban, S. Mustafa, A. El-Shihy, Finite-element modeling of externally posttensioned composite beams, J. Bridg. Eng. 20 (12) (2015), 04015018. https://doi.org/10.1061/(ASCE)BE.1943-5592.0000756.
[17] A. El-Zohairy, H. Salim, H. Shaaban, S. Mustafa, A. El-Shihy, Finite element analysis and parametric study of continuous steel–concrete composite beams stiffened with post-tensioned tendons, Adv. Struct. Eng. 21 (6) (2018) 933–945, https://doi.org/10.1177/1369433217732495.
[18] L.S. Moreira, J.B.M. Sousa, E. Parente, Nonlinear finite element simulation of unbonded prestressed concrete beams, Eng. Struct. 170 (2018) 167–177, https://doi.org/10.1016/j.engstruct.2018.05.077.
[19] A. Dall'Asta, A. Zona, Non-linear analysis of composite beams by a displacement approach, Comput. Struct. 80 (27) (2002) 2217–2228, https://doi.org/10.1016/S0045-7949(02)00268-7.
[20] G. Ranzi, A. Dall'Asta, L. Ragni, A. Zona, A geometric nonlinear model for composite beams with partial interaction, Eng. Struct. 32 (5) (2010) 1384–1396, https://doi.org/10.1016/j.engstruct.2010.01.017.
[21] R.E. Erkmen, M.M. Attard, Displacement-based finite element formulations for material-nonlinear analysis of composite beams and treatment of locking behaviour, Finite Elem. Anal. Des. 47 (12) (2011) 1293–1305, https://doi.org/10.1016/j.finel.2011.07.001.
[22] T. Hozjan, M. Saje, S. Srpčič, I. Planinc, Geometrically and materially non-linear analysis of planar composite structures with an interlayer slip, Comput. Struct. 114 (115) (2013) 1–17, https://doi.org/10.1016/j.compstruc.2012.09.012.
[23] N. Khorsandnia, H. Valipour, S. Foster, K. Crews, A force based frame finite element formulation for analysis of two and three layered composite beams with material non-linearity, Int. J. Non Linear Mech. 62 (2014) 12–22, https://doi.org/10.1016/j.ijnonlinmec.2014.02.001.
[24] P. Keo, Q.-H. Nguyen, H. Somja, M. Hjiaj, Exact finite element formulation for an elastic hybrid beam-column in partial interaction with shear-deformable encasing component, Eng. Struct. 125 (2016) 494–503, https://doi.org/10.1016/j.engstruct.2016.07.015.
[25] C.G. Chiorean, S.M. Buru, Practical nonlinear inelastic analysis method of composite steel-concrete beams with partial composite action, Eng. Struct. 134 (2017) 74–106, https://doi.org/10.1016/j.engstruct.2016.12.017.
[26] M.A. Uddin, A.H. Sheikh, D. Brown, T. Bennett, B. Uy, Geometrically nonlinear inelastic analysis of steel–concrete composite beams with partial interaction using a higher-order beam theory, Int. J. Non Linear Mech. 100 (2018) 34–47, https://doi.org/10.1016/j.ijnonlinmec.2018.01.002.

[27] J.B.M. Sousa Jr., C.E. Oliveira, A.R. da Silva, Displacement-based nonlinear finite element analysis of composite beam–columns with partial interaction, J. Constr. Steel Res. 66 (6) (2010) 772–779, https://doi.org/10.1016/j.jcsr.2009.12.015.
[28] J.B.M. Sousa Jr., C.F.D.G. Muniz, Analytical integration of cross section properties for numerical analysis of reinforced concrete, steel and composite frames, Eng. Struct. 29 (4) (2007) 618–625, https://doi.org/10.1016/j.engstruct.2006.06.002.
[29] D. Zupan, M. Saje, Analytical integration of stress field and tangent material moduli over concrete cross-sections, Comput. Struct. 83 (28–30) (2005) 2368–2380, https://doi.org/10.1016/j.compstruc.2005.03.030.
[30] M. Menegotto, P.E. Pinto, Method of analysis for cyclically loaded reinforced concrete plane frames, including changes in geometry and non-elastic behavior of elements under combined normal force and bending, Preliminary Report for Symposium on Resistance and Ultimate Deformability of Structures Acted on Well-Defined Repeated Loads, Vol. 13 of IABSE 1973, pp. 15–22.
[31] J. Ollgaard, R. Slutter, J. Fisher, Shear strength of stud shear connections in lightweight and normal weight concrete, AISC Eng. J. 8 (2) (1971) 55–64.